

**Reworking geometric morphometrics  
into a methodology of transformation grids**

Fred L. Bookstein  
University of Vienna, University of Washington

ORCID: 0000-0003-2716-8471

fred.bookstein@univie.ac.at, flbookst@uw.edu

This is an update of a manuscript of the same name and authorship that was submitted to *Evolutionary Biology* on January 2, 2023.

**Abstract.** Today’s typical application of geometric morphometrics to a quantitative comparison of organismal anatomies begins by standardizing samples of homologously labelled point configurations for location, orientation, and scale, and then renders the ensuing comparisons graphically by thin-plate spline as applied to group averages, principal components, regression predictions, or canonical variates. The scale-standardization step has recently come under criticism as unnecessary and indeed inappropriate, at least for growth studies. This essay argues for a similar rethinking of the centering and rotation, and then the replacement of the thin-plate spline interpolant of the resulting configurations by a different strategy that leaves unexplained residuals at every landmark individually in order to simplify the interpretation of the displayed grid as a whole, the “transformation grid” that has been highlighted as the true underlying topic ever since D’Arcy Thompson’s celebrated exposition of 1917. For analyses of comparisons involving gradients at large geometric scale, this paper argues for replacement of all three of the Procrustes conventions by a version of my two-point registration of 1986 (originally Francis Galton’s of 1907). The choice of the two points interacts with another non-Procrustes concern, interpretability of the grid lines of a coordinate system deformed according to a fitted polynomial trend rather than an interpolating thin-plate spline. The paper works two examples using previously published midsagittal cranial data; there result new findings pertinent to the interpretation of both of these classic data sets. A concluding discussion suggests that the current toolkit of geometric morphometrics, centered on Procrustes shape coordinates and thin-plate splines, is too restricted to suit many of the interpretive purposes of evolutionary and developmental biology.

**KEYWORDS:** Procrustes analysis, thin-plate spline, geometric morphometrics, Vilmann neurocranial octagons, anthropoid midsagittal crania, transformation grids, quadratic fits, bilinear maps, cubic fits, two-point shape coordinates, modularity, baseline registration, D’Arcy Thompson.

## I. Introduction

Figure 1 here arose simply as free play with the tools of geometric morphometrics (GMM). The data set comprises the familiar “Vilman octagons” tracing around the mid-sagittal neurocrania of close-bred laboratory rats radiographed in the 1960’s by the Danish anatomist Henning Vilman at eight ages between 7 days and 150 days and digitized some years later by the New York craniofacial biologist Melvin Moss. This version of the data is the one explored in my textbook of 2018: the subset of 18 animals with complete data (all eight landmarks) at all eight ages. The concern of Figure 1 is the contrast of the Procrustes-averaged shapes for the age-7 and age-150 animals (only the averages, no consideration of covariances). The heavy lines are for the age-150 data subset, the light lines, the data from the animals at age 7 days (a configuration this paper will occasionally refer to as the “template”). All panels of the figure complicate the usual Procrustes plot of shape coordinate pairs by all or some of the segments connecting these coordinate pairs. In the figure’s left column, all  $8 \cdot 7/2 = 28$  of the interlandmark segments have been drawn; in the right column, only the subset that are the reason for calling your attention to this figure. In the top row, those average locations correspond to the usual Procrustes-registered shape coordinates, partialling out only centering, size, and rotation. Panel (b) is limited just to the nine (out of 28) interlandmark segments from panel (a) that rotated either way by at least 8.6 degrees (the figure label expresses this as “0.15 radians”) <sup>1</sup> between age 7 and 150 days. A pretty graphic, but it features too much overlay of signals to qualify as a legible pattern analysis.

However, most of the clutter is due to the substantial change of aspect ratio (height-to-width ratio, obvious in the left column) that rotated both of the longer diagonals (Basion to Bregma, Lambda to SES) of the template. Fortunately, we already know how to remove this unwanted uniformity of relative vertical compression from our comparison: recourse to the “nonuniform” component of Procrustes shape space, complement to the subspace of uniform transformations (those that take all rectangles into parallelograms). The resulting plots are the pair in the bottom row.

It is no surprise that the diagram at lower left, panel (c), looks even more cluttered than panel (a), because now the calvarial roof, not just the cranial base, overlaps between the ages. But there is also a new signal once the diagram is edited to suppress all the segments that didn’t rotate much, a signal that seems not to have been anticipated in previously published analyses of these data. As panel (d) shows, six of the 28 possible segments rotate by more than 0.15 radian after standardizing this uniform aspect of the young-to-old comparison. And now the pattern is obvious. The five landmarks at left (anatomical posterior, SOS around to Lam) are rotating clockwise (in this projection) over growth, while the three at the right, located anatomically anteriorly, are rotating counterclockwise, all this to a longitudinal arrangement (think of the centroid of the set of five, versus the centroid of the frontmost three) that isn’t rotating either way. This paper will refer to the segmented polygon SOS-Bas-Opi-IPS-Lam, the set of five landmarks at

---

<sup>1</sup> One radian is the mathematician’s natural metric of angle, the angle (about  $57^\circ$ ) at which the extent of a circular arc is equal to the radius of the circle.

left in Figure 1(d), as the “posterior pentagon” and the remaining three, Brg-SES-ISS, as the “anterior triangle.”

The opposition of rotations in panel (d) is consistent with a report using an alternative arithmetic of intersegment length-ratios. There is evidently shortening of upper calvarial anteroposterior length, Lam to Brg, relative to the central segment of the cranial base from ISS to SOS. Now there is no need to state that this pattern is “relative to the sequestering of the uniform term,” as uniform transformations do not alter ratios of distances in the same direction, whether concurrent or parallel.

This relative rotation, including that contrast of vertically aligned horizontal growth rates, the central cranial base versus the calvarial roof above it, is surely a feature of the 143-day change of form here. But where is it to be found in the GMM toolkit? Figure 2 recovers exactly the same report from a quantitative style dating back more than 80 years prior to GMM, analysis via the coordinates Francis Galton introduced in 1907 for “classification of portraits.”<sup>2</sup> Here I have diagrammed every possible two-point registration of these octagons (quantified only by their average coordinates as Moss originally digitized them). For each alternative baseline, the original Cartesian coordinate average configuration has been separately rotated and scaled so that the first baseline point is at  $(0, 0)$  of a new coordinate system and the second is at  $(1, 0)$  in the same system (the two points circled in every panel of the figure). We have thereby altered every single step of the Procrustes toolkit — the centering, the rotating, the scaling — while eschewing any recourse to the thin-plate spline for separating out that uniform term. And yet ten of the panels clearly show the same phenomenon, the relative rotation between the anatomically posterior pentagon of landmarks and the anterior triangle. Whenever both ends of the baseline are in the same sector (here numbered [8,1,2,3,4] versus [5,6,7]), the rotation is clear in the behavior of the complementary sector. This is particularly evident in the analysis to baselines 5-6 (row 4 column 5), 5-7 (row 4 column 6), or 3-4 (row 3 column 2), where, regardless of any overall change of aspect ratio, the border of the octagon opposite the baseline appears to have radically shifted by a rotation with respect to that baseline. The disparity between ratios of change of length for segments ISS-SOS and Lam-Brg is clearest, perhaps, in the panel for that ISS-SOS baseline, fifth row, fourth column.

Such an analysis, both elegant and elementary, shares no arithmetic with the standard GMM toolkit of Procrustes registration and thin-plate splines. (For a good overview of computational aspects of that standard toolkit in a format suitable for routine biometric applications, see Claude 2008.) It is far older than that morphometric synthesis of the

---

<sup>2</sup> The GMM literature usually refers to these as “two-point coordinates” or an “edge registration,” while the statistical literature (Stuart and Ord 1994:279) calls them “Bookstein coordinates” in keeping with Stigler’s Law, which states that usually innovations are named after the second person to stumble across them. Ignoring the scaling aspect of this tool, the centering and orientation here was already explicit in Boas (1905) and probably can be traced back all the way to the German anthropologists’ adoption of the celebrated “Frankfurt Horizontal” in 1882 (see Garson, 1885 [which, remarkably enough, is available from JSTOR] — Orbital set to  $(0, 0)$ , Porion along the positive  $x$ -axis: the *Ohr-Augen Horizontale* of Martin 1914). For a contemporary critique of this specific convention of 1882, see Bookstein, 2016.

1990's, older even than analysis by triangles (“tensor biometrics,” Bookstein, 1984) or by biorthogonal grids (Bookstein, 1978). Both of these versions involve attention to short or long transects of the form that intersect *internally*, where, by analogy with the change of form from a square to a rectangle, for one particular pair of directions (sides of the square) the ratios of change of distance are greatest or least and the angle of intersection is invariant at  $90^\circ$ , while the ratio of change of the two distances at  $45^\circ$  to these directions (diagonals of the square) is unity and it is the change of their *angle* that is maximized. A closer inspection of the interlandmark-distance interpretation of Figure 1(d) instead makes reference to distances that are parallel at some spacing (upper calvarial width versus lower), a change visible equally in the Procrustes fits and in the two-point versions, especially versions 7-8 (row 5 column 4) and 3-5 (row 3 column 3). The idea of examining ratios of parallel distances like these is already present in some much earlier applied treatises, such as Martin 1914.

For an intuitive understanding of what is going on here, turn back to the earliest textbook introduction of the thin-plate spline, Bookstein 1991, where analyses like these, restricted to just a quadrilateral of landmarks, exemplify what I called “purely inhomogeneous transformations” there, meaning, transformations without any uniform component. Figure 7.3.6 of that book displays, within the limits of the software tools of the time, the effect of rotating the starting grid on the graphs of this purely inhomogeneous component (here, the sole nonlinear component) of the deformations of a square that minimize net bending energy — the now-ubiquitous thin-plate spline.

Figure 3 is a modification of that textbook figure intended to clarify the contrast of the different types of salience (length-ratios and rotations) for the pairs of segments of interest. Its four columns prototype different types of the transformations, each of a starting square of landmarks. In the top row are the starting squares, twice in Cartesian alignment with the page and twice at  $45^\circ$ . Below are the corresponding analyses, enhanced by ordinary thin-plate splines that are not actually part of the arithmetical report. (But that spline has nothing to do with the analysis here, which deals only with the landmark positions per se, not any interstitial tissue. The quadratic extension to the interstitial rendering in Figures 4 through 11 requires a minimum of six landmarks, not just these four; the further extension to a cubic fit in Figures 17 and 19 requires at least ten.) In column (a) the square is transformed to a rhombus by rotating two of its edges without change in length. What change are the angles between the concurrent edges. In column (b) the same transformation is applied to the square of landmarks at  $45^\circ$  (in other words, the grid has rotated with respect to the landmarks, the configuration of which has not changed in either row). Now the report is reversed: the greatest change is in the ratio of lengths of diagonals, while the angle between them is left invariant at  $90^\circ$ . This was also the case for the configuration in column 1, where it was confounded by the inconvenient orientation of the grid lines.

The situation in Figure 1(d) or Figure 2 corresponds instead to the prototype in columns (c) or (d) of Figure 3. The starting configuration is still the same square. But in column (c) the transformation changes the ratio of lengths of two edges that are *parallel* (horizontal in the figure), not perpendicular as in columns (a) or (b), while leaving unchanged the ratio of the other two edge lengths (the other pair of parallels in panel c1)

while radically altering their *angle*. This is a transformation from a square to an isosceles trapezoid. The complementary transformation in column (d), which the geometer would call square-to-kite, leaves the diagonals unchanged in length and in angle while altering the relation between their midpoints. Now it is a different pair of paired edges whose length-ratio has not changed — the top and bottom *V*'s — and while the angles at the end of the horizontal diagonal are hardly altered, those at the ends of the vertical diagonal are greatly changed, one increased and the other decreased. To repeat, these reports rely not at all on any GMM technology, neither Procrustes nor thin-plate spline.

The aim of this paper is to push this insight as far as it can go while remaining elementary in its biomathematics. (For instance, its multivariate analysis is limited to the familiar setting of multiple regression.) While the idea of two-point coordinates was originally Galton's in 1907, the idea at which the analysis here is aimed, the quadratic growth-gradient, is only half as old: it is present in embryo in Peter Sneath's underrated paper of 1967 on trend-surface analysis of D'Arcy Thompson's transformation grids. The core of the argument inheres in any of the next eight figures, which selected eight interesting baselines from the 28 in Figure 2 for expansion of the analysis to include an explicit quadratic regression of the averaged age-150 Cartesian coordinates against the same from the age-7 octagons. These analyses completely ignore the tools of standard GMM — there is no Procrustes centering, no scaling or reorientation beyond the (arbitrary) choice of baseline, and thin-plate splines are drawn only to be dismissed — while what results, you will see, is a coherent summary of this particular change of neurocranial form. A combined Figure 12 arrays the eight separate summaries for a synthesis of their information content abstracted in Figures 13 and 14. Following this exploration, a further analysis of some data from a study of cranial hominization my Vienna group published twenty years ago will consider some extensions of this approach, and a concluding Discussion will reflect on some implications of this seeming irrelevance of today's conventional GMM toolkit for the explanatory purposes of evolutionary or developmental morphology.

## II. Vilmann 7-to-150-day growth analyzed without Procrustes GMM

The recommended alternate analysis of the Vilmann growth gradient in Figure 1 may be narrated by an extraction of common findings from a suite of separate analyses to my selection of baselines, some transects of the octagon and others circumferential to it. The analyses to be synthesized are laid out in Figures 4 through 11.

Each of these eight composites offers four panels. At upper left will be the conventional thin-plate spline of the averaged octagon of Cartesian coordinates of the age-7-day animals as warped into the analogous average at age 150 days. Analysis is to the baseline of the pair of landmarks indicated in larger circles, which specifies the orientation of the thin-plate spline grid in each example. To its right will be a gridded version (in this orientation) of the “growth fit” likewise displayed first for comparison as a thin-plate spline. Here the  $x$ -coordinate of the deformed grid is the predicted  $x$ -coordinate from the regression of the baseline-standardized octagon vertices of the 150-day average on *both* coordinates of the age-7 average, and also their squares and their crossproduct (i.e., a regression of each  $x_{150}$  on  $(x_7, y_7, x_7^2, y_7^2, x_7y_7)$ ) and likewise the  $y_{150}$ -coordinates. Each of these regressions

involves five predictors, plus a constant, for only eight “cases” (the relevant coordinate,  $x$  or  $y$ , of the eight landmarks), and so has only two degrees of freedom for error; they are not really regressions, but rather almost interpolations, when the landmark count is so small. At left in the lower row will be a more appropriate representation of the quadratic fit splined at above right: actual transforms of the grid lines of the starting form to this baseline, with the regressions’ “dependent variable” the  $x$ - and  $y$ -coordinates of the filled dots corresponding to the fitted locations at the open circles nearby. Finally, the panel at lower right will restrict this grid to just the interior of the age-7 octagon — this portion of the graphic deserves attention first, before any extensions to the exterior.

Consider, then, the first figure in this series, Figure 4, which is the analysis for a baseline from Basion to Opisthion — the shortest interlandmark segment in the template, but one contained entirely within the posterior pentagonal compartment of Figure 1(d) and hence one that might enlighten us as to the rotation archived there. That rotation between anterior landmark triangle and posterior landmark pentagon is essentially the same that is displayed in Figure 1 for the conventional GMM approach and in Figure 2 for the panel corresponding to this baseline (there, the panel in row 1, column 1) — indeed it will be the same in all eight of the series of figures. Here in Figure 4, for the baseline Basion to Opisthion (axis of the midsagittal foramen magnum), the orientation of the form is rotated about  $130^\circ$  from the Procrustes convention in Figure 1. The thin-plate spline (upper left panel) is interesting in that inside the posterior five-landmark component, SOS around to Lam, the interior as rendered by the spline appears to be nearly affine (all grid cells the same size and shape) except near IPS, and likewise nearly affine for the anterior component Bas-SES-ISS. The growth fit (upper right panel) apparently has pulled IPS to the left in this diagram. As Figure 1 shows, and as has been explicated in earlier papers (e.g., Bookstein 2017), this point participates in a specific focal process displacing it upward in the more realistic anatomical setting of Figure 1. Thus the fit in this upper right panel of Figure 4 does not show the deviation of change at IPS from change at its neighbors that is present in the actual data.

Either panel of the lower row shows how closely the fitted landmarks (open circles) track the averaged 150-day locations observed (the solid circles). The horizontal grid lines in the interior of the form (lower right panel) are mainly straight, while their orientation on this diagram is graded from top to bottom more smoothly than one would infer from the analogous diagram at upper left (the thin-plate spline based on the fully detailed data record, which, by design, is not conducive to any lower-dimensional summary). The steady rotation of this imputed grid line direction is complemented by a gentle curvature of the *other* grid line direction, a curvature that is not so apparent in the explicit thin-plate spline at upper left — the transformation that appears segmented there, one nearly linear system for the posterior pentagon and another for the anterior triangle, is smoothed by the quadratic regression into a continuous gradient from end to end of the template (top to bottom of the grid, in this coordinate system). Note that the prediction error of the quadratic fit (lower row) specifically implicates the length of the chosen baseline, at both ends.

Figure 5 shows the same analysis for a different baseline, Basion to Interparietal suture, from the same posterior pentagon. Again the quadratic fit (lower row) shows a substantial

residual, this time at only one of the baseline points (IPS). In the deformed grid, both systems of lines are curved, a feature that makes interpretation more difficult.

Figure 6 is the first to involve a cross-component baseline, Basion (from the posterior pentagon) to Bregma (from the anterior triangle). The starting grid has rotated about  $80^\circ$  from its position in the first of this series (i.e., the angle between segments Basion-Opisthion and Basion-Bregma in the age-7 average is about  $80^\circ$ ). Again the panels in the lower row inform us that the initially vertical grid lines (lines along Lambda-ISS or IPS-SOS) are transformed by the quadratic fit into a pencil of nearly straight lines at varying orientations, while the lines of the originally orthogonal system are gently curved in a manner that will concern us in detail in Figure 13. At neither of the baseline points is there any substantial fitting error of the quadratic regressions. The approximate uniformity of cell sizes across the trimmed grid at lower right here and in every other figure of this series assures us that the recourse to distances from the centroid in models of centric allometry, such as Bookstein 2021a, is a reasonable default. Indeed the separation between the actual age-150 centroid and the quadratic trend transform of the age-7 centroid is a mere 0.054 units in the scale of this figure.

Figure 7, to a baseline from IPS to SOS, is very nearly the same analysis as in Figure 6 inasmuch as the two baselines, IPS-SOS and Bas-Brg, are nearly at  $90^\circ$  in the age-7 template. The main difference is the substantial increase in fitting error, owing to the fact that landmark 3, IPS, is known to be strongly loaded on a special factor not shared with the rest of the configuration. Nevertheless, the grids of the lower row still greatly resemble those of the preceding figure, for the baseline at  $90^\circ$  to this one: lines parallel to IPS-ISS (here, the baseline) remain straight but rotate from end to end, while the orthogonals are gently curved.

Let us move more quickly through the remaining versions of this four-panel scheme. In Figure 8, baseline Lambda-SOS, both systems of grid lines are gently curved (although the rotation from end to end of the original octagon is as clear as if they had remained straight). The errors of fit at the baseline points are moderate in magnitude, partly because the fit at Lambda is distorted by the need to accommodate the deviation at IPS.

Figure 9, for a baseline Bregma-SES within the *anterior* component of Figure 1, displays gentle curves in both grid systems. Errors of the quadratic fit are again moderate, and the rotation so evident in Figure 1(d) is very clear in spite of the curvature of these deformed grid lines. The baseline in Figure 10, Bregma-ISS, has similar errors of fit and similar curving of the grid lines. Finally, Figure 11, for an ISS-Bas baseline, is roughly the  $90^\circ$  rotation of the analysis in Figure 5, whose baseline (Bas-IPS) is roughly at  $90^\circ$  to the baseline here.

Figure 12 summarizes all eight of these analyses in a way that permits some criteria of interpretability to emerge regarding replacement of the Procrustes rotation by a protocol more conducive to reportage: a protocol that associates the reorientation of specimens to the ultimate simplification of their deformation by reference to the specific coordinate lines as deformed from the template's square grid. We have seen that baseline analyses can sometime come in pairs if the corresponding interlandmark segments themselves lie at approximately  $90^\circ$ , and it is better if they run close to the centroid of the octagon. More subtly, morphological comparisons that can result in reports of relative rotations of parts



of a landmark configuration may be diagrammed best not by a thin-plate spline but by a choice of a specific baseline that highlights the rotation in question, like Figure 6 or Figure 7 here, by leaving one set of grid lines straight lines even as they are rotated. (For instance, in Figure 6, the panel at lower right is more interpretable than the panel at upper left, even though the information content is effectively the same.) The thin-plate renderings in Figure 12, columns 1 and 3, all confirm the relative rotation detectable already in Figure 1, but do not otherwise appear to offer much intuitive accessibility. By comparison, the quadratic-fit displays, columns 2 and 4, vary enough in their legibility that some are truly insightful. Those that seem most helpful are the pair of analyses in the second row, to baseline Bas-Lam or IPS-SOS (two directions that happen to be nearly perpendicular) — these seem to be considerably better than the standard GMM analysis at showing a potentially meaningful gradient for the growth process being visualized here.

The analysis in Figure 7 suggested a scenario I have highlighted in Figure 13 by the simple trick of extending the domain of the quadratic fit beyond the bounds of the landmark locations being fitted. The diagram here extends the earlier gridded transformation merely by evaluating it on the new real estate to the left in the same template coordinate system, i.e. into the empty space some distance above the foramen magnum of these animals, where the horizontal grid lines of Figure 7 appear to be converging. We see that the near-linearity of the transformation along the baseline and all the grid lines parallel to that direction persists quite far beyond the actual anatomical limits of the comparison, resulting in the strong impression of some sort of descriptive center at an unphysiological distance outside the actual calva. The apparent rotation suggested in Figure 1(d) is embedded here in a larger system of reorientations that might be viewed as continuous rather than segmented, or, in a more suggestive language, graded rather than modular. The suggestion is strong, for instance, that this grading ought to be checked for extending further anteriorly to the facial skeleton (a description that will be tied to the classic interpretation of “orthocephalization” by a footnote in Section IV) or other features outside of this particular neurocranial data set.

Figure 14 sketches two geometrical interpretations of Figure 13, one more familiar to the applied mathematician and the other less so. Each is an alternative to the thin-plate spline of column (d) in Figure 3; one will prove more realistic than the other for this paper’s examples. The more familiar map is the *projection*, central panel, that takes every straight line onto another straight line. But this mapping substantially alters the spacing of the points where these deformed grid lines meet the bounding kite. No such respacing appears in the extended quadratic fit itself, Figure 13. An alternative better matching that observed quadratic fit is the family prototyped in the right-hand panel of the figure, the *bilinear map* that I discussed in considerable detail in Bookstein 1985. Bilinear maps<sup>3</sup> take one quadrilateral onto another as follows. Every point  $(x, y)$  in the interior of the template quadrilateral is the intersection of two lines connecting opposite edges that divide those edges in the same ratio. The map takes  $(x, y)$  to the intersection of the two lines that divide the homologous pair of edges in the target in the same ratio. The bilinear map of square onto kite can be written  $(x, y) \rightarrow (x, y) + a(1 + xy, 1 + xy)$  for some  $a$ . The projection

---

<sup>3</sup> In finite-element analysis, these are often called *isoparametric coordinates* of the quadrilateral.

in Figure 14 required the upper isosceles triangle of the template to be mapped into the space above the horizontal diagonal of the kite, entailing a considerable compression of its vertical coordinate; the bilinear transformation enforces much less compression here, at the cost of bending that horizontal diagonal over the course of the deformation. This attenuation of the variability of those ratios of area change seems to match the graphics of all the quadratic fits in Figures 4 through 11 after an appropriate rotation.

Returning one final time to the scheme in Figure 1(d), the decomposition of the neurocranial octagon into two nonoverlapping components, we see that the figure has indeed oversimplified the situation there. That the rotation of all edges of the posterior pentagon leaps to the viewer’s eye obscures the fact that all but one of these segments have changed their *length*. And likewise the anterior “triangle,” Brg-SES-ISS, does not rotate rigidly — its edge from SES to ISS shortens and also does not rotate as far as the other two. Any report focusing on the two “components” is deficient in failing to refer to the coordinate space in-between them, where the unconformity between anteroposterior changes of length along the cranial base versus along the calvarial roof seems better captured by the rotating lines of the Bas-Brg baseline and IPS-SOS baseline analyses (Figure 12, row 2, columns 2 and 4) than by the irregularities of the corresponding thin-plate splines (columns 1 and 3).

### III. An example from hominization of the skull

The Vilmann analysis of Section II exploited the best study design that experimental zoomorphology has to offer: a sample of close-bred animals imaged by identical machinery at a fixed sequence of developmental ages. (The identification of this research design as the *summum bonum* of laboratory evo-devo research is a century old — it dates from no later than Przibram 1922.) Most of the data structures to which GMM has been applied are not so elegantly designed. This paper’s final example is a pair of comparisons, each much more typical in its design, that share one 20-landmark configuration scheme. The data are a selection from the 29 forms analyzed in Chapter 4 of Weber and Bookstein (2011) that originated in computed midsagittal sections of a larger sample of CT scans digitized by Philipp Gunz for the growth analysis in Bookstein et al. (2003). That original analysis explicitly relied upon the same GMM toolkit that is most commonly invoked today: Procrustes analysis, principal components of the resulting shape coordinates, and visualizations by thin-plate spline.<sup>4</sup>

Of the specimens homologously digitized in 2003, most are *Homo sapiens*, while four are named specimens of *H. neanderthalensis* (Atapuerca, Kabwe, Guattari, and Petralona), and two are specimens of *Pan*, one of each sex. For the present reanalysis I have averaged the 18 adult *sapiens* (one of which, Mladeč, is an archaic specimen) and, as a separate group, the four neanderthals. As a third “group” (present for a didactic purpose, a com-

---

<sup>4</sup> In one version or another these data have already been used for demonstrations of GMM in textbooks three different times: not only Weber and Bookstein (2011) but also Bookstein (2014, 2018). The approach circumventing those typical GMM maneuvers is new to the present paper.

parison of comparisons) I selected the female adult chimpanzee, because the adult male shows even more of the heterochrony that will render my final figure so extreme in certain aspects of its geometry. Of course these samples are far more limited than any data resources that would be brought to bear on the same comparisons today. It would be unreasonable to claim that the computations to be reported presently are valid empirical findings; my purpose is instead to demonstrate a methodological alternative to Procrustes- and spline-based GMM.

The left panel of Figure 15 names these twenty landmarks at their positions in the average of the *H. sapiens* sample in the original CT coordinates, which were not far from a Sella-Nasion orientation. In the right panel this configuration is supplemented by the configurations of the same twenty points for the female chimpanzee and also for the neanderthal average, all after the two-point transformation (Bookstein coordinates) that put all three ANS's (of which two are group averages) at  $(0, 0)$  and all three internal Lambda's at  $(1, 0)$ . Evidently this coordinate system has been rotated, translated, and scaled from the panel at its left, but none of these steps proceeded by the Procrustes method.

Consider first the analysis in Figure 16, which in its design echoes three of the four panels of the Vilmann series, Figures 4 through 11, but in this case only for one selected baseline, from ANS to LaI, as in the right panel of Figure 15. (Analysis to a roughly perpendicular baseline, Opi-BrI, results in essentially the same diagrams.) The comparison in Figure 16 is from the averaged points for *H. sapiens* in Figure 15 to the averaged points for *neanderthalensis*. In both of these *Homo* averages (and also in the single female adult *Pan* specimen to come) the baseline crosses the cranial base near Sella roughly halfway along its length. The thin-plate spline deformation from the average of the eighteen humans to the average of the four neanderthals, upper left in the figure, shows the expected contrast of shrinking neurocranium and expanding splanchnocranium, particularly along the palate; the cranial base interposes itself as the so-called "hafting zone." As the upper-right panel shows, this grid is tracked to some extent by the analogous grid for the fitted values of the same *neanderthalis* landmarks from the quadratic regression on the *sapiens* coordinates. That quadratic regression, already demonstrated many times in the Vilmann example preceding, shows most of its failure of fit (discrepancies between the open circles and their filled neighbors in the lower-left panel) along that central separatrix, with a possible exception at lower right where the pairings of the two inions are rearranged in both separation and orientation. As Figure 15 hinted, this rearrangement is due mainly to excessive variation at InE, external inion.

The final quadratic trend grid, at lower left in Figure 16, is strikingly different from the thin-plate spline of the same point loci (upper right). Indeed this grid for the fit looks remarkably like a rotation of the grid at right in Figure 14, the bilinear transformation leaving two specific families of straight lines straight after the deformation, while their orientations rotate across the diagram. At this large scale, the comparison of midsagittal crania of these sister species is largely smooth — the points in the hafting zone differ hardly at all from their predicted locations under the quadratic analysis. In particular, the implication of modularity in the upper right panel is completely effaced in the actual quadratic fit grid at lower left, indicating instead an approximating spatial process that is homogeneously graded with no natural boundaries embryological or otherwise. The grading

is consistent with the observation that relative to the face the neanderthal neurocranium is smaller than that of *sapiens* with some relative rotation as well.

Figure 17 analyzes the same comparison by a cubic fit instead of the quadratic fit in Figure 16. (Specifically, this fit models each of the twenty  $x$ -coordinates of the *H. neanderthalensis* average and then each of its twenty  $y$ -coordinates as a linear combination of *nine* terms  $x_{sap}$ ,  $y_{sap}$ ,  $x_{sap}^2$ ,  $y_{sap}^2$ ,  $x_{sap}y_{sap}$ ,  $x_{sap}^3$ ,  $y_{sap}^3$ ,  $x_{sap}^2y_{sap}$ , and  $x_{sap}y_{sap}^2$ . The quadratic regressions used only the first five of these predictors.) These cubic grids show bizarre behavior outside the limits of their driving data (the strange cusps already clear in Sneath's examples of 1967), so as in the Vilmann exposition of Section II I extended the figure by one more panel, lower right, that trims the grid to just the interior of the region occupied by the actual target configuration (here the *H. neanderthalensis* average). The straight lines of the rendering in Figure 16 now appear as S-curves across that same hafting zone, and of course the new fit, a regression on nine predictors, has to be closer than that in Figure 16 based on only five of the nine. But the change of size-ratios between neurocranium and splanchnocranium remains clear, as does the directional extension along the palate and the relative rotations from anterior to posterior and from caudal to cranial.

The situation is quite different for the comparison of the *H. sapiens* average to our more distant relative, the female chimpanzee. The quadratic analysis analogous to Figure 16 can be found in Figure 18, but it no longer appears to look entirely like the bilinear map of Figure 14. Instead we encounter a strong *local* feature of the transformation, the apparent flattening of the parietal region, that is seen in both of the thin-plate spline renderings of the top row (at left, for the actual shape coordinates; at right, for the quadratic fit) and likewise in the gridded representation of that quadratic fit at lower left. Strikingly, the residuals of this analysis seem no greater than those of the comparison of the *sapiens* sample with the neanderthals, Figure 16, yet the flattening of the splines is clearly detected by this quadratic fit as well, which has so many fewer coefficients (and also a matrix inversion step of much lower rank,  $5 \times 5$  instead of  $23 \times 23$ ). The bidirectional linearity of the lower left panel in Figure 16 has certainly ceased to apply globally, while the hafting zone here seems still to be no sort of natural boundary between multiple modules. The deformation remains smoothly graded except locally, in the parietal region.

Yet when we switch the algorithm from the quadratic (five-term) fit to the cubic (nine-term) fit, Figure 19, nothing essential changes in the analysis as a result of these additional four degrees of freedom per coordinate. The thin-plate spline of the fitted points (upper right panel) is not much altered from that in the previous figure except in that same nonconforming parietal region, and while the cubic fit here leads to pathologies of the extrapolated grid at every corner of the original scheme (lower left panel), its restriction to the interior of the actual anatomy, lower right in the figure, shows grid lines that, ignoring their curvature, are actually well-aligned with those of the lower left panel in Figure 16, the comparison from *sapiens* to *neanderthalensis*. We have thereby confirmed graphically that the shape difference in the parietal region is indeed *local*. Put this another way: the quadratic fit (Figure 18) and the cubic fit (Figure 19) convey the same message, a relatively continuous gradient of deformation right across the hafting zone. And they agree, too, that the situation at the parietal (landmarks Opi through LaE) is *not* coherent with this large-scale gradient. From Bregma forward, the lower right panels in Figures 17

and 19 differ mainly in the intensity of rotation of these gridline segments; but posterior to that arbitrary boundary the parietal landmarks participate in a reorganization that is incommensurate between the two comparisons.

Thus we see again that, just as in the Vilmann growth example, an approach that eschews all of the standard Procrustes steps and also the usual thin-plate spline is capable of generating the same understanding of a morphological phenomenon, in this case a somewhat more complicated one.

## IV. Discussion

A. *The main concern of GMM ought to be the transformation grid per se.* This was already clear from the earliest formal appearance of the concept in D’Arcy Thompson’s *On Growth and Form* (Thompson, 1917), where the review literature usually begins (even though portrait artists like Albrecht Dürer had thought about this much earlier). The endpoint of the method ought to be not statistical but graphical, and the derived report should be geometrical, not statistical, en route to an ultimately biophysical or otherwise morphogenesis-informed endpoint. The main dilemmas in this tradition were already well-critiqued over the first six decades of its development as I reviewed them in Chapter 5 of Bookstein, 1978. No matter how clearly defined the positions of individual landmark points might be, there was no complementary rhetoric for reporting meaningful features of the transformation grid that expressed comparisons of their configurations over meaningful biological contrasts. The best exposition of *this* problem remains Sneath, 1967, a paper that struggled, ultimately unsuccessfully, to bring the algebra of landmark analysis (in that pre-spline era) into alignment with the reasoning of numerical taxonomy. Yet D’Arcy Thompson would have been delighted with the grid in Figure 13, while presentations of the same information in Procrustes style, Figure 1a, or spline-style, panels 4(a) through 11(a), would have been of no use to him at all. A more contemporary and quite distinct tradition of transformation studies approaches the problem via a calculus of *diffeomorphisms* (see, for example, Grenander and Miller, 2007), which makes no essential reference to landmarks at all, instead basing its computations on the full field of image contents, gray-scale or even colored, spanning the organ(s) of interest. The approach seems particularly helpful in neurological applications to imagery of the human brain. This contrasting method, however, is beyond the scope of my Procrustes critique here.

The analysis in Figure 7 suggests renewing Thompson’s original concern in this domain, the interpretation of grids per se, via injecting a new theme into the discussion, an anatomical basis for orienting the starting grid on the template, that more intensively exploits the interaction between deformation graphics and the investigator’s prior awareness of how coordinate systems themselves can vary in their visually dominant features. The biomathematics ought to begin, then, with a confluence of two insights: one, that *some* morphological domains might be amenable to *some* kind of functionally interpretable large-scale pattern analysis, and the other, an intuition about the geometrical language by which the pattern of interest might be quantified. For Henning Vilmann, this translation began with the knowledge that growth of rodent neurocrania is a plausible domain for morphometric exploration and that its midsagittal aspect bears enough information about growth

and function to be worthy of geometrization not only in his own measurements of extent, nor the numerous intermediate multivariate investigations of this same data set (including several of my own), but also in the novelties of Section II. But given these two axioms, an applied study would culminate in an exploration not of alternative *statistics* but of alternative *graphics*: a survey not of diverse linear combinations but of diverse grid renderings. Information about absolute scale change, where relevant (as in biomechanical aspects of interpretation), can be embedded in any of these grid figures by a simple magnification over the course of printing, or can be inscribed on interlandmark segments or the line-elements of a transformation grid by overprinting. In this context of large-scale comparison, rotation is a tool of rendering clarification, not a nuisance variable of digitizing.

The quadratic regressions in Figures 4 through 11 all used the same list of five predictors  $x, y, x^2, y^2, xy$ . This consistency lets the renderings here, unlike the approach in the lower row of Figure 1, preserve the uniform component of the transformation grid, where we can see how it interacts with these gradients of large but finite scale. But the directions corresponding to those two axes  $x$  and  $y$  vary from baseline to baseline, and the baseline points are not privileged by the regressions. Consequently the coordinates pinned by the two-point registration are not quite pinned by the regression — they are permitted to shift to some extent from solid to fitted circles in the grid figures here.

The resulting dataflow sheds new light on what we mean by “*the best rotation*” when, as in both of this paper’s examples, different parts of an organ appear to rotate relative to one another over a comparison of interest. The role of the multiple two-point registrations that this paper recommends as a substitute for the Procrustes algorithm is not itself a “finding” of any sort but merely a convenience, a simple way of regularizing the landmarks’ Cartesian coordinates in order that a selection of reasonable polynomial trends can be fitted, each in a reasonably equably weighted way. Its advantage is that unlike the case for the Procrustes method, there is more than one of them. The Procrustes approach optimizes a quantity (sums of squares of landmark shifts) that is irrelevant to the ultimate purpose of an evolutionary or developmental GMM analysis, which is not a minimized sum of squares or a singular-value decomposition or a classification but rather a plausible biological hypothesis for the observed form-differences, their causes, or their consequences for the organism.

Then the logic of the inference engine we need is not the operationalized Procrustes arithmetic itself, the least-squares fit to what is almost always a completely wrong model (the null model, a pure similarity transformation). Instead we need the logic of E. T. Jaynes’s approach to numerical inference (e.g., Jaynes 2003): the explicit acknowledgement of what we do *not* know — what is missing from the list of data-driven constraints on some quantitative empirical inference. (I have recently reviewed this logic in the rather different context of paleoseismology, which is the history of great earthquakes — see Bookstein 2021b.) What is missing from a Procrustes analysis is, among other things, the acknowledgement that choice of an orientation constraint affects the resulting report: what we seek is the orientation that will best clarify the final published diagram. Furthermore, regardless of this issue of orientation, in every GMM context we already know there is no “correct” registration, because there is no “correct” list of landmarks — in the presence of any regional rotation or rescaling, different lists of landmarks or semilandmarks lead

to different Procrustes registrations, and the empirical report of a shape comparison must accommodate that specific form of ignorance. That is the whole purpose of the grids — to free our attention from the landmark data per se to the space in-between where biological processes actually take place.

The particular protocol dictating the selection of orientations to be considered may be irrelevant to the quantitative morphological inference under study. (Recall that in this paper the two points fixed in the baseline registration are not fixed by the fitted trend — the registration is not an inferential component of the grid report at all.) Orientation may be specified as any interlandmark segment from the available pairings, or any homologous boundary alignment, or even a specific force vector such as a muscle load or gravitational vertical — or possibly all of these. Whatever the choices of orientation, the investigator of a global deformation is led to the approach here, which is the selection of at least one satisfactory such orientation as judged by the ultimate diagram at the end of the workflow. In 3D, one could proceed via an assortment of large landmark triangles passing near the centroid, similarly searching for clarity and redundancy. But in other contexts that issue of orientation may be quite relevant to the interpretation. The examples here have all dealt with global trends, but Figures 18 and 19 hinted at a need for a deformation tool suitable for local features as well. Such a tool would likewise entail a rotation of the Cartesian coordinate system prior to grid computation, but in general a different one — see, for example, the model of the *crease* in Bookstein 2000 or Bookstein 2014, Figure 7.19.

*B. We need to broaden the range of ideas we borrow from geometry.* A combination of two branches of geometry led us to the bilinear interpretation in Figure 14 of the grid in Figure 13, but this other toolkit is not among those currently being taught to biomathematicians. The kernel  $r^2 \log r$  of the thin-plate spline doesn't much resemble the biological processes we are trying to understand, but the algebra of polynomial fits (here, mainly the specific appearance of bilinear maps leaving both pencils of coordinate lines almost straight and almost evenly spaced after deformation) does pick up much of the classic appearance of growth-gradients as laid out for analysis from Thompson on. More important than the extension of the idea of a coordinate system, though, is an extension of the domain of morphometric data to include empirical entities other than landmark points. The description of the grid in Figure 13 makes no essential mention of *any* of the landmarks — the simple exegesis here (bilinear reorganization of that particular family of grid lines while remaining lines) pertains much more to the interior of this octagon (the directions of those transects across it, or, if you will, the pairing of points across the left and right sides of the outline in this orientation) than to any of its boundary delineation detail, even though that boundary is the sole data source for the example. Thus at root the finding exemplifies a language of intraorganismal matching, the pairing of points along a shared curve bounding some anatomical entity in section. Pairings like these are not like landmarks in any formal aspect.

So even though this paper's first example argument began from a playful GMM-derived diagram, Figure 1d, it ends up formalized in the rhetoric of a spatial extension (Figure 13) unknown to GMM but comprehensible by every reader of Thompson's chapter, as interpreted in Figure 14 via a similar-looking figure from a subchapter of college geom-

etry. This logical sequence can be reversed: beginning from those same textbooks, to try finding biological examples that illustrate them. We are used to polar coordinates, for example (most recently in the study of centric allometry, Bookstein 2021a), but what about bipolar coordinates or confocal coordinates (Bookstein 1981, 1985) and other schemes that (literally) co-ordinate position with respect to two origins or two axial systems at the same time? The range of coordinate systems is vastly broader than the Cartesian on which today's GMM automatically relies. My biorthogonal grids (Bookstein 1978) already went beyond this possibility, though not in a statistically feasible way, via their formalism of one-axis and three-axis singularities corresponding to the "lemon" and "star" umbilics that are the topic of advanced treatises such as Koenderink (1990). From the earliest years of the twentieth century the mathematics of geometry has permitted us to talk about coordinates of many different extended structures: not just points, but lines, planes, circles, and many other formalisms. See, at first, Hilbert and Cohn-Vossen, 1931/1952, and then, among the more contemporary surveys, Porteous 2001 or Glaeser 2012.

Thus the word "geometric" in the phrase "geometric morphometrics" needs to have its meaning broadened beyond the current focus on the Procrustes component of GMM or indeed any version based on analysis of landmark points as logically separate data elements. "Procrustes distance" between specimens, when computed as a minimizing sum of squared Cartesian coordinate differences, is just a theory-free proxy for the far more subtle and multifarious concept the biologist knows as the opposite of "similarity," and today's GMM treats Procrustes shape coordinates as just a list of Cartesian pairs (or triples) in their own coordinate space of position, without reference to any explicit features for describing how their interrelationships (e.g. the interlandmark segments of Figure 1) actually change across a comparison of configurations. D'Arcy Thompson got this correct back in 1917: "The deformation of a complicated figure," he wrote (Thompson 1961:271), "may be a phenomenon easy of comprehension, though the figure itself have to be left unanalyzed and undefined. This process of comparison, recognizing in one form a definite permutation or deformation of another, apart altogether from a precise and adequate understanding of the original 'type' or standard of comparison, lies within the immediate province of mathematics."

That geometry of "recognizing deformation" is not limited to the geometry of points referred individually to Cartesian axes. Thompson himself referred explicitly to the appearance of the deformed grid lines in his drawings. For the comparison to *Mola*, for instance, he wrote, "I have deformed [*Diodon*'s] vertical coordinates into a system of concentric circles, and its horizontal coordinates into a system of curves which, approximately and provisionally, are made to resemble a system of hyperbolas" (Thompson 1961:300). It is the configuration of these curves, not the landmarks on them, that is the bridge from arithmetic to understanding. In other words, the elementary language of deformation, the language by which we report morphological comparisons as deformations, must be based in a glossary of multiple elementary types of deformable image components, not disarticulated landmarks. The roster of these is broad indeed, including, among other options, the changes of point-pairs to other point-pairs at a different distance or direction that we already saw in Figure 1, but also changes of triangles to other triangles, squares to any quadrilateral whether rectangle, parallelogram, trapezoid, or some other form, displace-



ment of interior points with respect to an unchanging boundary, circles to ellipses, ellipses to any other simple closed curve, straight lines to other straight lines, lines to any other open curve, line-elements having an orientation in the small as well as a location (for a spline cognizant of this structure, see Bookstein and Green, 1993), or nearby pairs of parallel lines to any bent ribbon tracing the sequence of changes all along their shared length. All of these have appeared in biometric examples; each requires a different geometric grammar for its reporting. For instance (in another acknowledgement of our sister discipline of neuromorphometrics), line elements per se summarize image data for the method known as diffusion tensor analysis that traces and summarizes patterns of wiring in the human brain.

As I hope you have already come to suspect from the figures in this paper, the thin-plate spline is not designed to be of any particular help in this matter. Its functional form is mainly a sum of terms  $r^2 \log r$ , where  $r$  is the distance from each grid point to each landmark of the template in turn, and so it has no machinery for collecting references to two or more landmarks at the same time, but must revert to the nonbiological symmetries of linear multivariate statistics for this purpose (so that the partial warps, for instance, are just a  $(2k - 4)$ -dimensional rotation of its Cartesian coordinates however they were arrived at to that point, while the relative warps are just a different  $(2k - 4)$ -dimensional rotation of the same coordinates). No, the elements of a quantitative morphometric comparison in terms of deformation must be the whole coordinate systems of our deformation diagrams, and the features we extract must be features that refer to those deformed lines and areas, whether end to end or truncated to the vicinity of specific landmark subsets. Any geometric report qualified to drive a programme like Thompson's aimed at simple descriptions of relationships among individually complicated specimens must begin with more complicated elementary entities than positions of discrete landmark points. A search for such explananda, beginning from the paired interlandmark segments in Figure 1, leads immediately to the elementary aspects of this paper's two examples, which make no reference to the formula  $r^2 \log r$  nor indeed any quantification beyond the squaring or cubing of coordinates and products of those powers that allows us to parameterize families of nearly parallel curves that began as parallel lines.

*C. The exterior of an organ or an organism is a useful domain for communication of findings even in the absence of tissue.* This comment has real bite for a GMM that depends on the conventional thin-plate spline, which does not understand exteriors at all. So the usual interpolating spline is precisely the wrong tool for detecting large-scale gradients that, like the one summarizing the Vilmann comparison, are not affine — are not conducive to descriptions emphasizing some pair of directions at  $90^\circ$  bearing the maximum ratio of rates of change. Because the conventional thin-plate spline relaxes to uniform at great distances, it is not a helpful component of answers to any question about large-scale organization of a form-comparison, the question asked by most morphologists (and dysmorphologists, and paleontologists) ever since Thompson's time. To quantify the cunning hint from Figure 1d, I needed the tool of a quadratic trend surface (i.e., a fit, not an interpolation), and when the graphic of that fit proved intriguing, a suitable summary arose only when the rendering was extended (Figure 13) far enough beyond the actual convex hull of the landmarks that

Figure 14 could show us how to report its structure. However vague the language might be for a discussion of Figure 7 by itself, the reworking that is Figure 13 makes the implicit explicit — the extended grid now is exactly the report we seek, no actual words required except the legend explaining how the graphic was produced. But such a graphic no longer resembles any sort of conventional GMM output.

Because the interior of any non-nested module is at the same time a part of the exterior of every other module, one sees from the hominization example that the morphometric aspect of “modularity,” whatever its exact morphogenetic definition, is a matter not of landmark coordinates but of what happens to coordinate grid lines. Figures 17 and 19 confirm that, within the limits of these data resources (adult forms only, no growth series, a mere 20 landmarks), there is no graphical evidence for the cranial base as a separatrix between braincase and face, in spite of their obvious differences in function, but strong evidence for a separation of the whole anterior two-thirds of this landmark scheme from the five parietal landmarks, Opi through LaI and LaE, that so clearly seize control of the lower-right corner of the grids for either the quadratic fit (Figure 18 lower left) or the cubic fit (Figure 19 lower right) to the comparison across genera. While the empirical import of this second data example is obsolete, owing to advances in the accrual of samples of all these species, the practice whereby consideration of the transformation grids per se might shape inferences from landmark data about morphogenetic control processes ought to be transferred from the current GMM toolkit to these more integrated investigative tools along the lines of the examples here.

*D. The implications of a diminished role for the existing core of geometric morphometrics in quantitative morphology are liberating.* Via a new toolbox that intentionally discards Procrustes centering, Procrustes scaling, and Procrustes orientation, and that downplays the role of thin-plate splines — the whole core of today’s GMM — we may be able to better achieve GMM’s principal declared purpose, the quantitative understanding of morphological variation and its causes or effects, by recourse to more diverse geometrical formalisms, some ancient and some relatively novel. This methodological possibility has several implications, some for actual analysis of morphologies and others for the methodological component of graduate curricula in the evo-devo sciences. The aspects of geometry that GMM is accustomed to borrowing for its tools concentrate much too heavily on matrix algebra and linear multivariate analysis. As Peter Sneath suspected so long ago in his paper on trend-surface analysis, there are other geometric entities, such as those here dealing with quadratic bivariate polynomials, that speak more clearly to the investigator’s visual instincts, especially as regards phenomena of orientation. (Examine, for instance, panel 1d of Sneath 1967,<sup>5</sup> which shows a relative rotation between face and braincase in the comparison of *Homo* to *Pan* similar to the one in Figure 18 here, without, however, the optimization of coordinates that Section III exploited.) And far more objects can be assigned coordinates than discrete points (or semilandmarks) alone: grid lines, for instance, deserve coordinates of their own (Figures 4 through 11) and also interlandmark segments

---

<sup>5</sup> According to Biegert 1957, the orientation is along the central plane of the sphenoid (in Latinate German, “Planum-sphenoideum-Ebene”) to suit the needs of a much broader study of the midsagittal skull across the order *Primates*.

(Figure 1).

Similarly, the way GMM relies on thin-plate splines for its published renderings exaggerates their importance for organismal biology. The spline is an interpolating map, whereas, in view of how arbitrary our landmark lists actually are, biological interpretation often goes deeper and better via approximating maps instead. The actual role of interpolating splines in the research cycle, then, might be shifted well earlier, all the way back to before the final rendering style is chosen, in order to supply guidance about which geometrical languages should be exploited for the most effective dissemination. At that early stage, interpolating splines are good aids to the search for component processes that are primarily local, but are poor at the analogous global reports, which, as Sneath already knew in 1967, do better with polynomial analyses. Both possibilities should be checked, and perhaps both preserved in the final analysis, the way Figures 4 ff. show both the thin-plate spline, which reveals the local change at IPS, and the quadratic grid, which summarizes the overall change of form so much better (in both contexts ignoring the Procrustes side of GMM in favor of the different optimization of orientation recommended here).

The finding in Figure 1d should not have been new to this paper. In the many previous GMM investigations of the Vilmann data there should long since have been mention of rotations of subanatomies, a rhetoric that has been suppressed, perhaps unintentionally, by virtue of our current traditions of overly symmetric data summaries like Procrustes distance, principal component analysis and interpolating splines.<sup>6</sup> It is time for the morphological side of biomathematics to return to its roots in biological geometry *sensu lato* — what might the organism’s function space “know” about its own form? — in order to rebuild the interplay between data and explanation using a much broader range of geometric formalisms than just “points” (or their “modules”) and “deformations.” The method of cubic regression, Figures 17 and 19, is likewise not new; I copied it straight from Sneath (1967). The particularly careless way the Procrustes method dismisses orientation as just a nuisance variable has blinded our field to the possibility that relative intraspecimen orientations can be just as informative a channel of insight and explanation as relative extents (proportions). To restore and then extend this symmetry we need to abandon the standard Procrustes tool in favor of explorations that explicitly consider multiple orientations at the same time, just as studies of allometry have been considering multiple size measures since at least Blackith and Reyment (1971). More generally, to understand transformation grids we must extend our understanding of the sort of entities that can *have* coordinates from points to more extended structures. Only then can we trust our diagrams to provide straightforward practical summaries of the “blooming, buzzing confusion” (W. James) that is the spectrum of Darwinian phenomena we call evo-devo.

**Acknowledgements.** I thank Jim Rohlf, Stony Brook University, for thoughtful

---

<sup>6</sup> In an ironic exception, a non-Procrustes analysis in my 1991 textbook refers to this rotation as an epiphenomenon (a side-effect) of *orthocephalization*, the usual name for the process by which the anterior cranial base thrusts under the facial skeleton — but the verb “rotate” itself is in scare quotes! See Bookstein (1991:312).

commentary on the basic thrust of this manuscript at several earlier stages. It was Joe Felsenstein, University of Washington, who first alerted me to foundational problems in the way GMM handles the concept of “rotation.”

**Competing interests and funding.** There has been no support from any external funding source, and no conflicts of interest thereby.

## Literature Cited

Biegert, J. Der Formwandel des Primatenschädels. *Gegenbaurs morphologisches Jahrbuch* 98:77–199, 1957.

Blackith, R. E., and R. A. Reyment *Multivariate Morphometrics*. Academic Press, 1971.

Boas, F. The horizontal plane of the skull and the general problem of the comparison of variable forms. *Science* 21:862–863, 1905.

Bookstein, F. L. *The Measurement of Biological Shape and Shape Change*. Lecture Notes in Biomathematics, vol. 24. Springer-Verlag, 1978.

Bookstein, F. L. Coordinate systems and morphogenesis. In *Morphogenesis and Pattern Formation*, ed. T. G. Connelly, L. Brinkley, and B. Carlson. Raven Press, 1981, pp. 265–282.

Bookstein, F. L. Tensor biometrics for changes in cranial shape. *Annals of Human Biology* 11:413–437, 1984.

Bookstein, F. L. Transformations of quadrilaterals, tensor fields, and morphogenesis. In *Mathematical Essays on Growth and the Emergence of Form*, ed. P. L. Antonelli. University of Alberta Press, 1985, pp. 221–265.

Bookstein, F. L. Size and shape spaces for landmark data in two dimensions. (With Discussion and Rejoinder.) *Statistical Science* 1:181–242, 1986.

Bookstein, F. L. *Morphometric Tools for Landmark Data: Geometry and Biology*. Cambridge University Press, 1991.

Bookstein, F. L., and W. D. K. Green. A feature space for edgels in images with landmarks. *Journal of Mathematical Imaging and Vision* 3:231–261, 1993.

Bookstein, F. L. Creases as local features of deformation grids. *Medical Image Analysis* 4:93–110, 2000.

Bookstein, F. L., P. Gunz, P. Mitteröcker, H. Prossinger, K. Schäfer, and H. Seidler. Cranial integration in *Homo*: Singular warps analysis of the midsagittal plane in ontogeny and evolution. *Journal of Human Evolution* 44:167–187, 2003.

Bookstein, F. L., and P. M. Mitteroecker. Comparing covariance matrices by relative eigenanalysis, with applications to organismal biology. *Evolutionary Biology* 41:336–350, 2014.

Bookstein, F. L. *Measuring and Reasoning: Numerical Inference in the Sciences*. Cambridge University Press, 2014.

Bookstein, F. L. Reconsidering “The inappropriateness of conventional cephalometrics.” *The American Journal of Orthodontics* 149:784–797, 2016.

Bookstein, F. L. A method for factor analysis of shape coordinates. *American Journal of Physical Anthropology* 64:221–245, 2017.

Bookstein, F. L. *A Course of Morphometrics for Biologists*. Cambridge University Press, 2018.

Bookstein, F. L. Centric allometry: Studying growth using landmark data. *Evolu-*

*tionary Biology* doi:/10.1007/s11692-020-09530-w, 48:129–159, 2021a.

Bookstein, F. L. Estimating earthquake probabilities by Jaynes’s method of maximum entropy. *Bulletin of the Seismological Society of America* 111:2846–2861, 2021b.

Claude, J. *Morphometrics with R*. Springer, 2008.

Galton, F. Classification of portraits. *Nature* 76:617–618, 1907.

Garson, J. G. The Frankfort craniometric agreement, with critical remarks thereon. *Journal of the the Anthropological Institute of Great Britain and Ireland*, 14:64–83, 1885.

Glaeser, G. *Geometry and its Applications in Arts, Nature, and Technology*. (English edition, modified from the German original.) Springer, 2012.

Grenander, U., and M. Miller. *Pattern Theory: from Representation to Inference*. Oxford University Press, 2007.

Hilbert, D., and D. Cohn-Vossen. *Anschauliche Geometry*. 1931. Tr. by P. Nemenyi as *Geometry and the Imagination*, Chelsea Pub. Co., 1952.

Jaynes, E. T. *Probability Theory: the Logic of Science*. (Ed. G. L. Bretthorst.) Cambridge University Press, 2003.

Koenderink, J. *Solid Shape*. MIT Press, 1990.

Martin R. *Lehrbuch der Anthropologie in systematischer Darstellung*. Jena: Gustav Fischer, 1914.

Porteous, I. R. *Geometric Differentiation for the intelligence of Curves and Surfaces*, 2nd ed. Cambridge, 2001.

Przibram, H. *Form und Formel im Tierreiche. Beiträge zu einer quantitativen Biologie I–XX*. Franz Deuticke, 1922.

Sneath, P. H. A. Trend-surface analysis of transformation grids. *Journal of Zoology, London* 151:65–122, 1967.

Stuart, A., and K. Ord. *Kendall’s Advanced Theory of Statistics*. Volume 1, *Distribution Theory*. Wiley, 1994.

Thompson, D’A. W. *On Growth and Form*. Macmillan, 1917. Abridged edition, ed. J. T. Bonner, Cambridge University Press, 1961.

Weber, G. W., and F. L. Bookstein. *Virtual Anthropology: a Guide to a New Interdisciplinary Field*. Springer Verlag, 2011.

## Captions for figures

**Figure 1.** Unexpected pattern in the much-analyzed Vilmann data set of neurocranial octagons for growing laboratory rats. (upper left) Saturated network of interlandmark segments, Procrustes average shapes of the octagons at ages 7 days (light lines) and 150 days (heavy lines). Landmarks: Bas, Basion; Opi, Opisthion; IPS, Interparietal suture; Lam, Lambda; Brg, Bregma; SES, Sphenoëthmoid synchondrosis; ISS, Intersphenoidal synchondrosis; SOS, Sphenoöccipital synchondrosis. (upper right) Subnetwork of segments rotating by at least 0.15 radians ( $8.6^\circ$ ) over this age comparison. (lower left) The same saturated network for the nonaffine component only of the same Procrustes shape coordinates, with

landmark numbers. (lower right) Now that the uniform component of this shape coordinate space has been partialled out, there emerges a considerably simpler subnetwork, explicitly displaying the relative rotation of the anteriormost three landmarks with respect to the other five.

**Figure 2.** Two-point superpositions (Bookstein coordinates) of the Vilmann age-7 and age-150 average octagons for every possible baseline. Landmarks are numbered as in Figure 1. Circled landmarks: ends of the baseline as registered to (0,0) and (1,0). Light lines, age-7 average; heavy lines, age-150 average.

**Figure 3.** Contrasting morphometric renderings for diverse transformations by thin-plate spline (lower row) of a variously oriented square (upper row). (a) Square to parallelogram, grid aligned with the edges of the square. (b) The same, grid now aligned with the square's diagonals. (c) Square to trapezoid. (d) Almost the same, grid rotated 45°: square to kite. Adapted from Bookstein, 1991, Figure 7.3.6.

**Figure 4.** This is the first of eight figures that all have the same four-panel format as applied to one of eight selected baselines from the array of 28 offered in Figure 2. Top-row panels, left to right: actual change of averaged Cartesian coordinates, with thin-plate spline oriented to selected baseline; ordinary thin-plate spline of the quadratic fit to the age-150 average as regressed on first and second powers of the  $x$ - and  $y$ - coordinates of the template and also their product  $xy$ . Bottom row, left, the quadratic fit (not a spline) as a grid of its own. Solid circles, the observed data; open circles, predictions from this regression. Bottom right: restriction of the display list of grid vertices to the interior of the age-7 octagon as explained in the text. The baseline of this figure runs from Basion to Opisthion (landmark 1 to landmark 2).

**Figure 5.** The same as Figure 4 for a baseline from Basion to Interparietal suture, landmark 1 to landmark 3.

**Figure 6.** The same for a baseline from Basion to Lambda, landmark 1 to landmark 5.

**Figure 7.** The same for a baseline from Interparietal suture to Sphenoöccipital synchondrosis, landmark 3 to landmark 8. Each panel is roughly a 90° rotation of the corresponding panel in Figure 6, having a baseline at about 90° to this one.

**Figure 8.** The same for a baseline from Lambda to Sphenoöccipital synchondrosis, landmark 4 to landmark 8.

**Figure 9.** The same for a baseline from Bregma to Sphenoöethmoid synchondrosis, landmark 5 to landmark 6.

**Figure 10.** The same for a baseline from Bregma to Intersphenoidal suture, landmark 5 to landmark 7.

**Figure 11.** The same for a baseline from Sphenoöethmoid synchondrosis to Basion,

landmark 6 to landmark 1.

**Figure 12.** Synthesis of upper left and lower right panels of Figures 4 through 11, analyses to eight of the 28 possible two-point baselines. Clearly some of these choices lead to simpler reports than others do. As the thin-plate spline is covariant with similarity transformations of its target, all the splines here (columns 1 and 3) are the same except for grid orientation and spacing. But the regressions associated with columns 2 and 4 weight different landmarks differently (in particular, weighting the two ends of the baseline not at all), so these grids can vary in more aspects than the baseline orientation per se.

**Figure 13.** Graphical extension of the quadratic fit to the IPS-SOS baseline yields a striking reinterpretation of the phenomenon. Left, grid extended to the left over the baseline-registered template; right, corresponding version of the fitted quadratic trend from Figure 7. Filled dots, observed average configurations after the two-point registration (left, age 7 days; right, age 150 days). Open dots, fitted values of the quadratic regression as in the earlier figures.

**Figure 14.** Two alternatives for column (d) of Figure 3. The map in Figure 13 more closely resembles the bilinear map (far right panel) than the projection map (central panel). The projection map sends *all* straight lines to other straight lines; the bilinear map, in general, only the lines that join matched proportional aliquots from opposite edges. In both deformations the dashed line delineates the effect of the map on the horizontal diameter of the starting diamond shape. The projection takes this curve to a straight line, the bilinear map, to a parabola engendering a less extreme reduction of the template cells' areas above this diameter. Owing to the shared symmetry axis of square and kite there is another set of straight lines within the grid in the rightmost panel — the verticals — but this third set is not present in the general case, hence the “bi” of “bilinear,” and so I have not drawn them here.

**Figure 15.** Landmark configurations for the hominization example, Section III. (left) Abbreviated names of the twenty landmarks printed at the raw digitized coordinate averages of the adult *sapiens* subsample of Bookstein et al. (2003). Alv, alveolare, inferior tip of the bony septum between the two maxillary central incisors; ANS, anterior nasal spine, top of the spina nasalis anterior; Bas, basion, midsagittal point on the anterior margin of the foramen magnum; BrE, BrI, external and internal bregma, outermost and innermost innermost intersections of sagittal and lambdoidal sutures; CaO, canalis opticus intersection, intersection point of a chord connecting the two canalis opticus landmarks with the midsagittal plane; CrG, crista galli, point at the posterior base of the crista galli; FcE, foramen caecum, anterior margin of foramen caecum in the midsagittal plane; FoI, fossa incisiva, midsagittal point on the posterior margin of the fossa incisiva; Gla, glabella, most anterior point of the frontal in the midsagittal; InE, InI, external and internal inion, most prominent projections of the occipital bone in the midsagittal; LaE, LaI, external and internal lambda, outermost and innermost intersections of sagittal and lambdoidal sutures; Nas, nasion, highest point on the nasal bones in the midsagittal plane; Opi, opisthion, midsagittal point on the posterior margin of the foramen magnum; PNS, posterior nasal spine, most posterior point of the spina nasalis; Rhi, rhinion, lowest point of the internasal



suture in the midsagittal plane; Sel, sella turcica, top of dorsum sellae; Vmr, vomer, sphenobasilar suture in the midsagittal plane. (right) Bookstein coordinates to an ANS-LaI baseline for the averaged adult *H. sapiens* and *H. neanderthalensis* samples and the single adult female chimpanzee.

**Figure 16.** Three grid diagrams for the comparison of the averaged *H. sapiens* and *H. neanderthalensis* twenty-landmark configurations, to an ANS-LaI baseline. (upper left) Conventional thin-plate spline grid deforming the *sapiens* average to the *neanderthalensis*. (upper right) Thin-plate spline rendering of the deformation from the same averaged *sapiens* to the quadratic regression fits (regressions on first and second powers of the  $x$ - and  $y$ -coordinates and also their product  $xy$ ) of the *neanderthalensis* configuration. (lower left) Explicit grid of that quadratic regression. Solid circles, observed averaged *neanderthalensis* two-point coordinates; open circles, fitted locations.

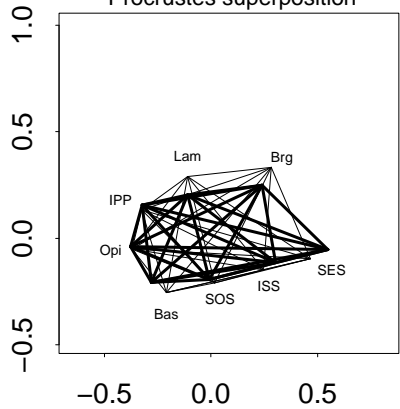
**Figure 17.** The same for a cubic regression of the *neanderthalensis* coordinates, nine predictors instead of five. Upper left, upper right, and lower left panels as in Figure 16. At lower right, an enlarged version of the fitted grid (lower left) as trimmed to the interior of the actual *neanderthalensis* average.

**Figure 18.** The same as Figure 16 for the comparison of the averaged *H. sapiens* to the single female chimpanzee in the data base of Bookstein et al. 2003.

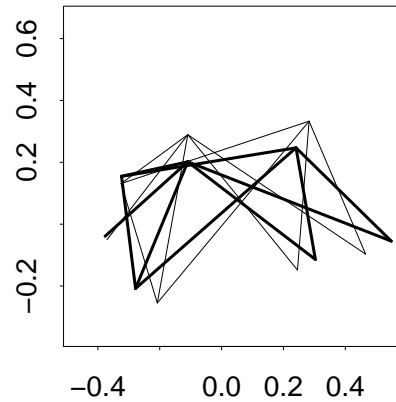
**Figure 19.** The same as Figure 18 for the comparison of *H. sapiens* to the female *Pan* using these tools. The grid at lower left, for the cubic fit, is correctly drawn even though it looks like a whale.

Figure 1.

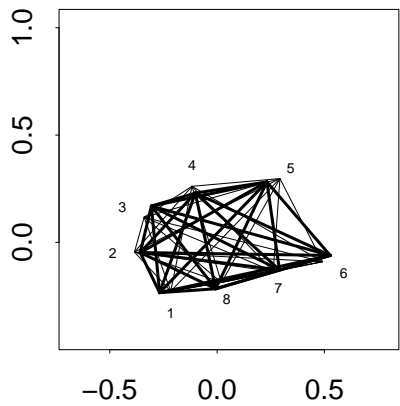
(a) average Vilmann octagons, 7 and 150 days, Procrustes superposition



(b) cut at rotation 0.15 radians



(c) the same, nonaffine component only



(d) the same, cut at 0.15 radians

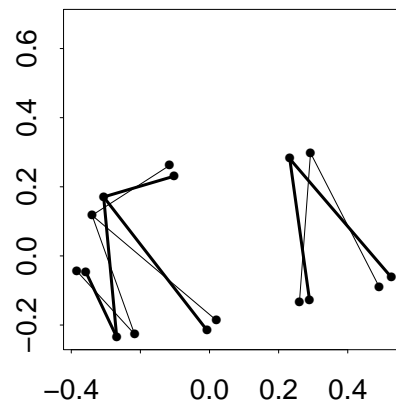
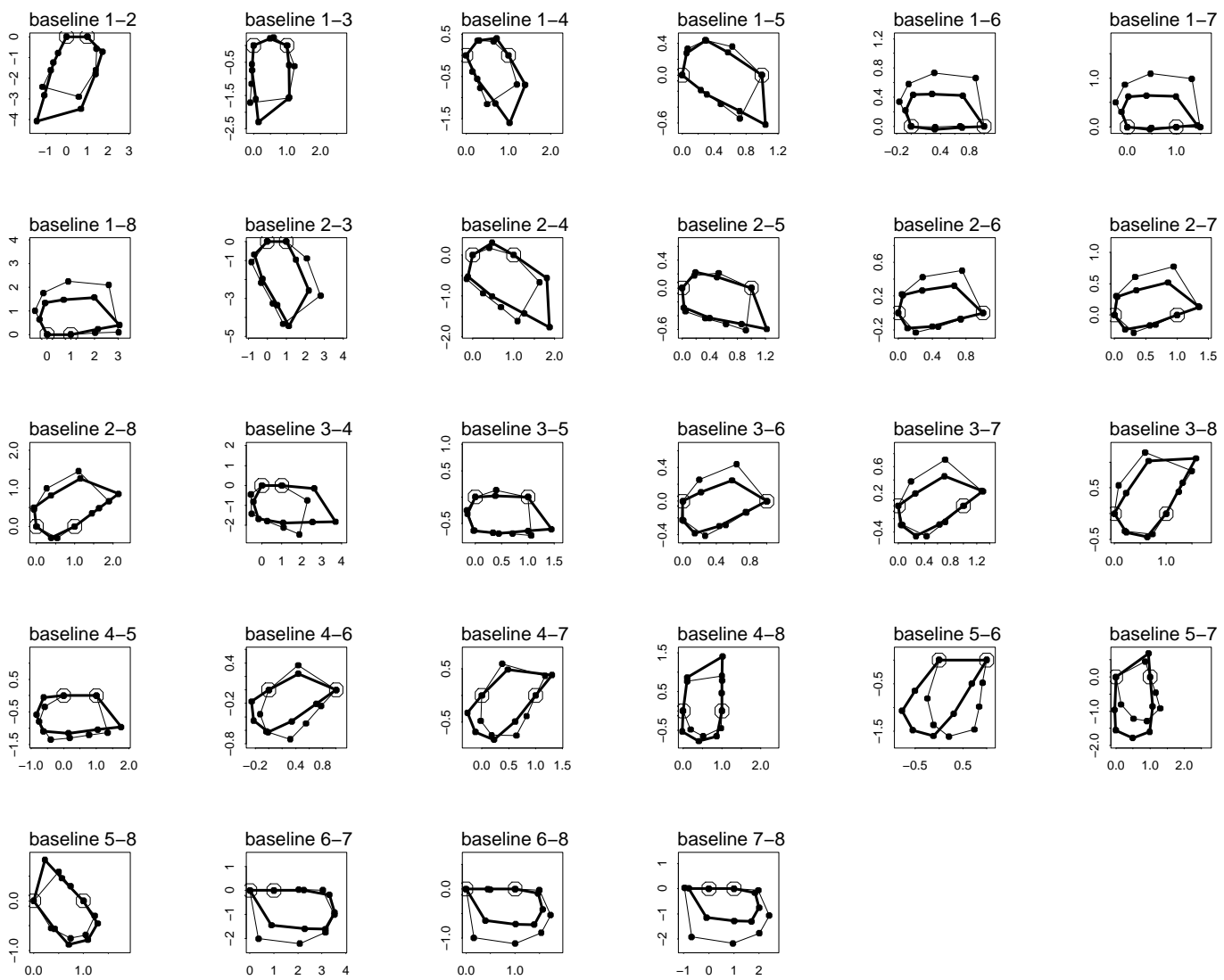


Figure 2.



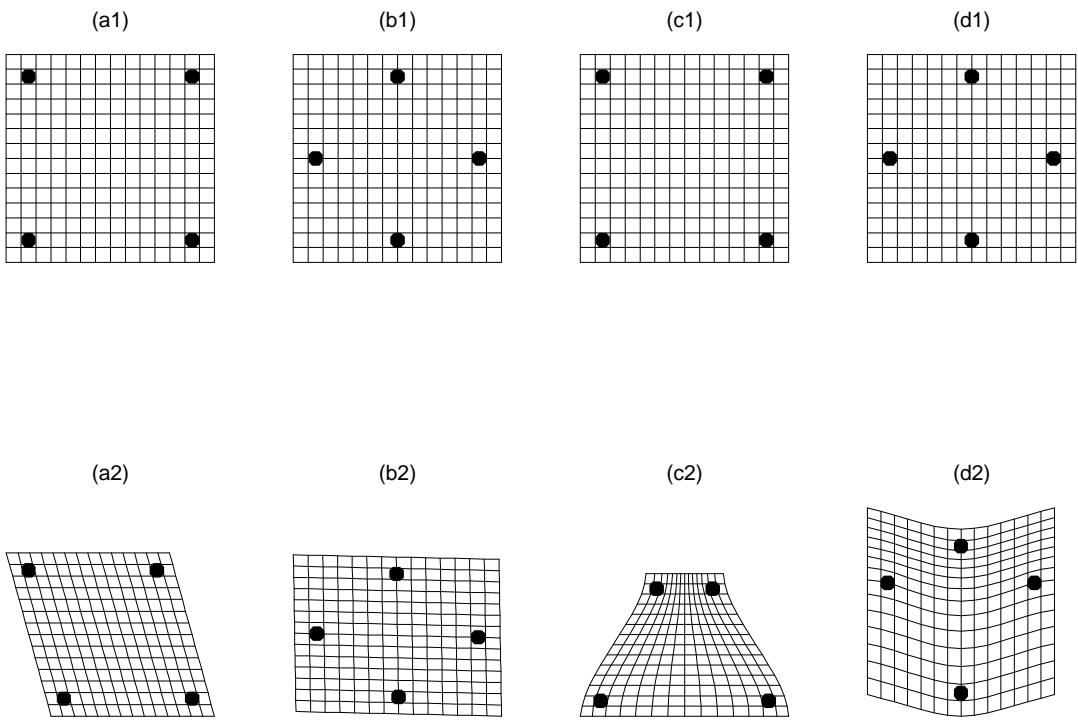
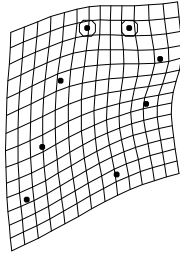
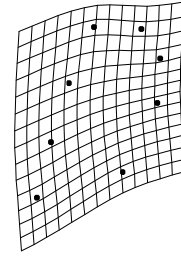


Figure 3.

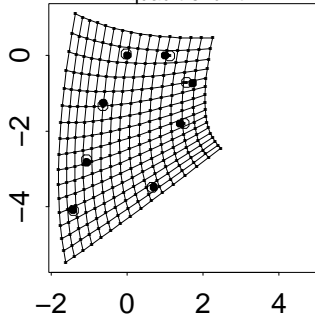
tps of actual growth, 7 days to 150,  
baseline 1 to 2



Vil 7-da to 150-da, baseline 1 to 2  
tps of growth fit



Vil 7-da to 150-da, baseline 1 to 2  
quad trend fit



Vil 7-da to 150-da, baseline 1 to 2  
quad trend fit, interior

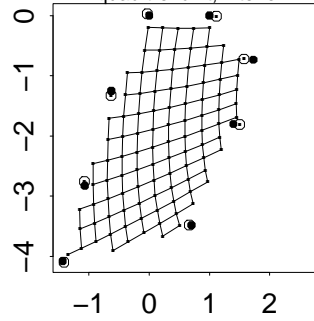
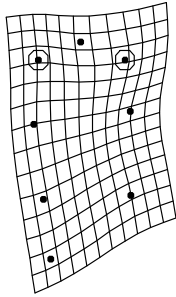
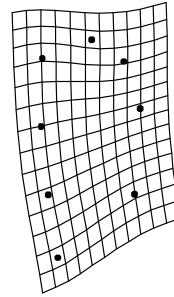


Figure 4.

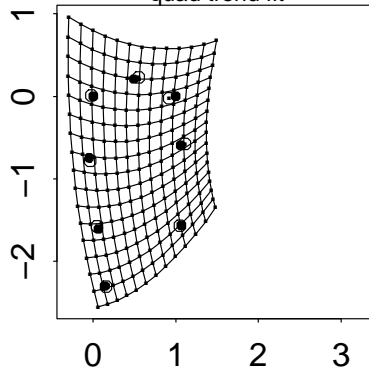
tps of actual growth, 7 days to 150,  
baseline 1 to 3



Vil 7-da to 150-da, baseline 1 to 3  
tps of growth fit



Vil 7-da to 150-da, baseline 1 to 3  
quad trend fit



Vil 7-da to 150-da, baseline 1 to 3  
quad trend fit, interior

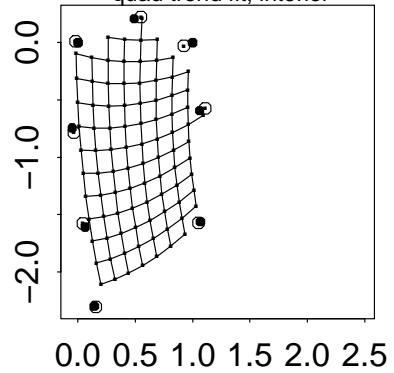
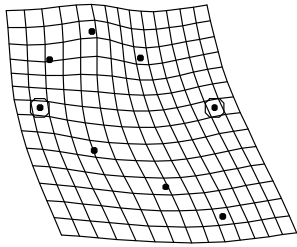
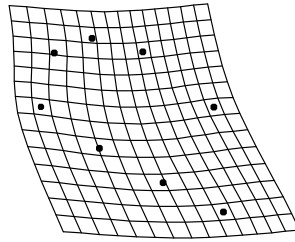


Figure 5.

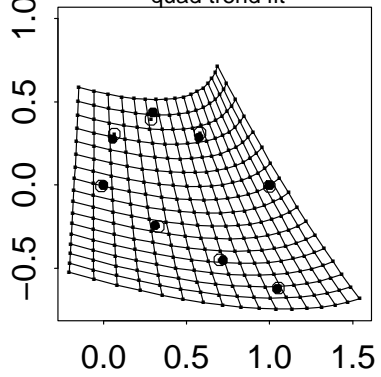
tps of actual growth, 7 days to 150,  
baseline 1 to 5



Vil 7-da to 150-da, baseline 1 to 5  
tps of growth fit



Vil 7-da to 150-da, baseline 1 to 5  
quad trend fit



Vil 7-da to 150-da, baseline 1 to 5  
quad trend fit, interior

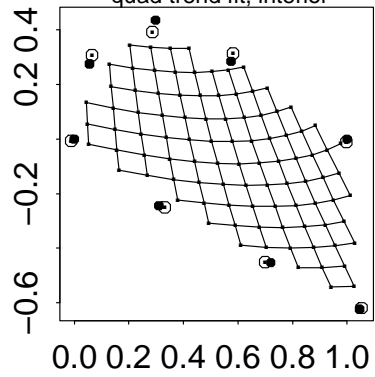
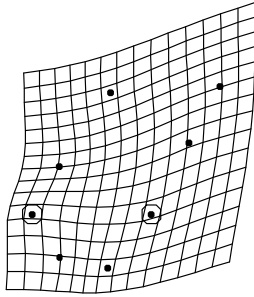
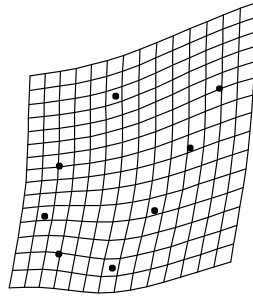


Figure 6.

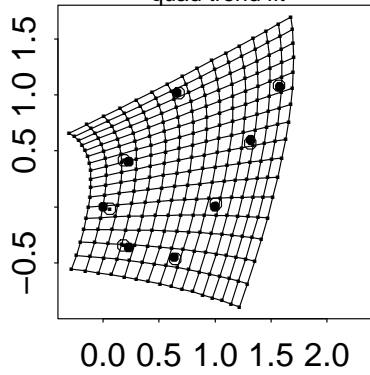
tps of actual growth, 7 days to 150,  
baseline 3 to 8



Vil 7-da to 150-da, baseline 3 to 8  
tps of growth fit



Vil 7-da to 150-da, baseline 3 to 8  
quad trend fit



Vil 7-da to 150-da, baseline 3 to 8  
quad trend fit, interior

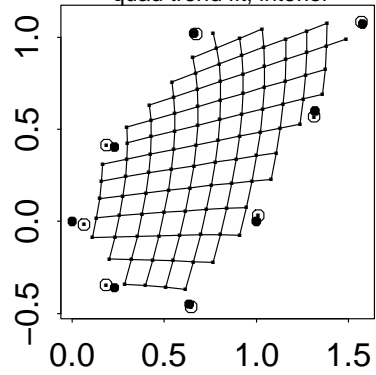
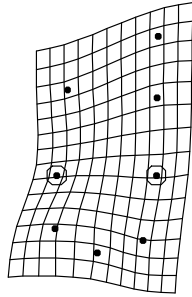


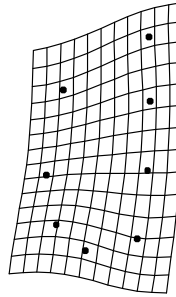
Figure 7.



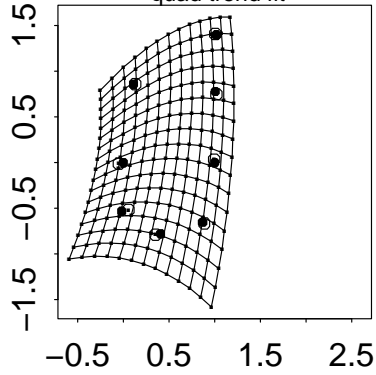
tps of actual growth, 7 days to 150,  
baseline 4 to 8



Vil 7-da to 150-da, baseline 4 to 8  
tps of growth fit



Vil 7-da to 150-da, baseline 4 to 8  
quad trend fit



Vil 7-da to 150-da, baseline 4 to 8  
quad trend fit, interior

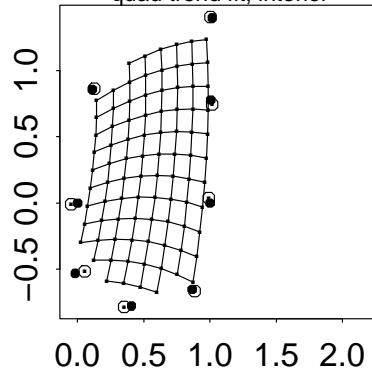
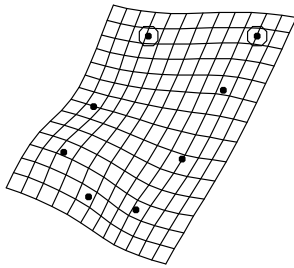
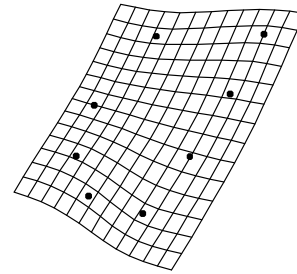


Figure 8.

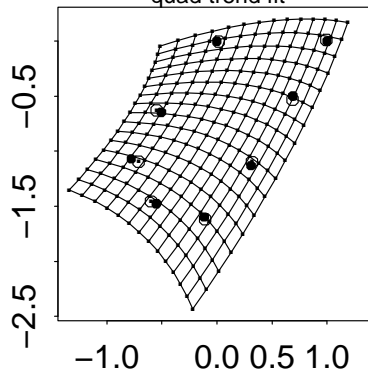
tps of actual growth, 7 days to 150,  
baseline 5 to 6



Vil 7-da to 150-da, baseline 5 to 6  
tps of growth fit



Vil 7-da to 150-da, baseline 5 to 6  
quad trend fit



Vil 7-da to 150-da, baseline 5 to 6  
quad trend fit, interior

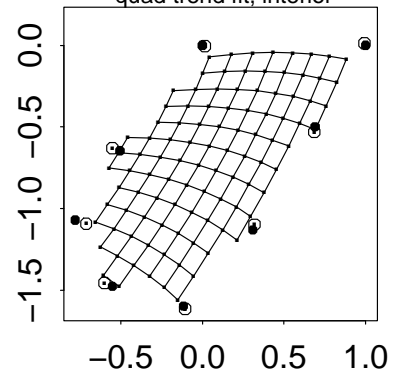
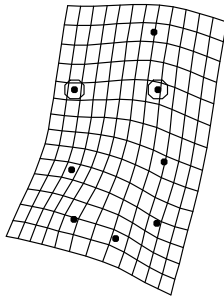
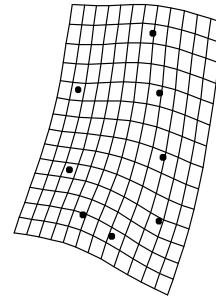


Figure 9.

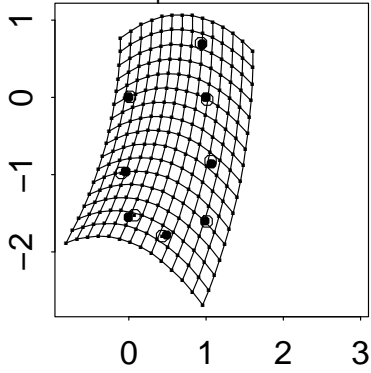
tps of actual growth, 7 days to 150,  
baseline 5 to 7



Vil 7-da to 150-da, baseline 5 to 7  
tps of growth fit



Vil 7-da to 150-da, baseline 5 to 7  
quad trend fit



Vil 7-da to 150-da, baseline 5 to 7  
quad trend fit, interior

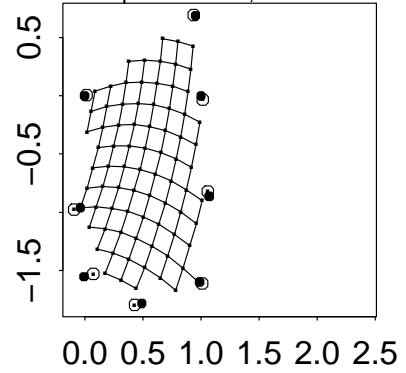
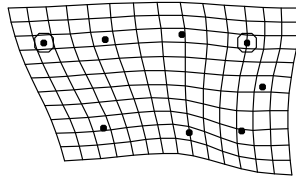
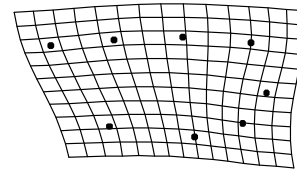


Figure 10.

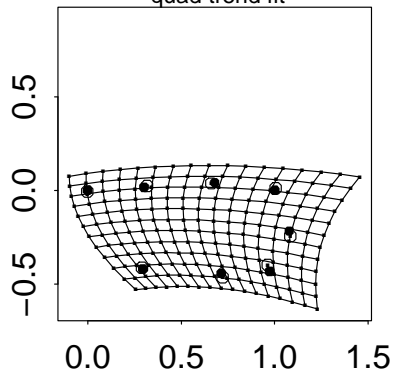
tps of actual growth, 7 days to 150,  
baseline 6 to 1



Vil 7-da to 150-da, baseline 6 to 1  
tps of growth fit



Vil 7-da to 150-da, baseline 6 to 1  
quad trend fit



Vil 7-da to 150-da, baseline 6 to 1  
quad trend fit, interior

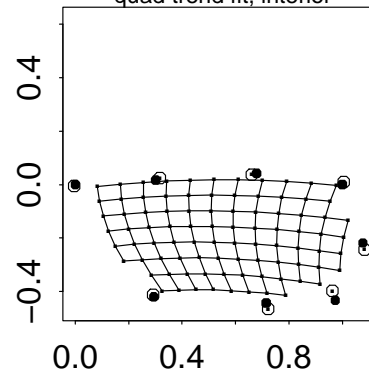
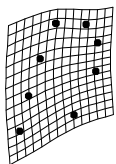


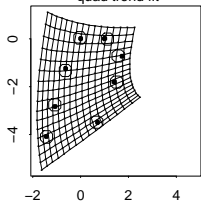
Figure 11.

Figure 12.

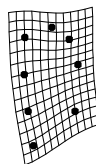
Vil 7-da to 150-da, baseline 1 to 2  
tps of growth



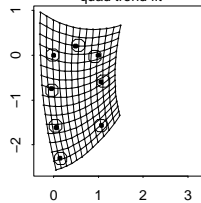
Vil 7-da to 150-da, baseline 1 to 2  
quad trend fit



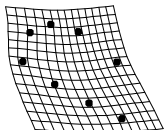
Vil 7-da to 150-da, baseline 1 to 3  
tps of growth



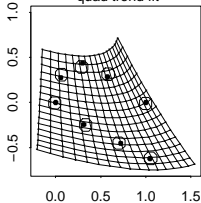
Vil 7-da to 150-da, baseline 1 to 3  
quad trend fit



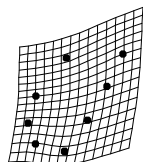
Vil 7-da to 150-da, baseline 1 to 5  
tps of growth



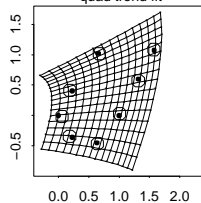
Vil 7-da to 150-da, baseline 1 to 5  
quad trend fit



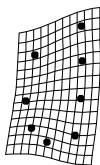
Vil 7-da to 150-da, baseline 3 to 8  
tps of growth



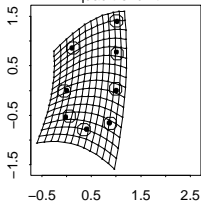
Vil 7-da to 150-da, baseline 3 to 8  
quad trend fit



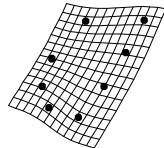
Vil 7-da to 150-da, baseline 4 to 8  
tps of growth



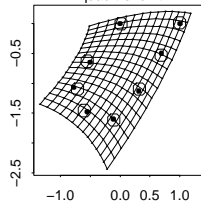
Vil 7-da to 150-da, baseline 4 to 8  
quad trend fit



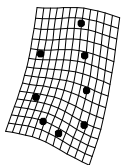
Vil 7-da to 150-da, baseline 5 to 6  
tps of growth



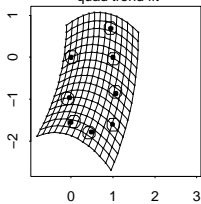
Vil 7-da to 150-da, baseline 5 to 6  
quad trend fit



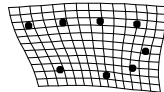
Vil 7-da to 150-da, baseline 5 to 7  
tps of growth



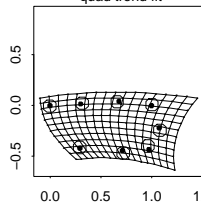
Vil 7-da to 150-da, baseline 5 to 7  
quad trend fit



Vil 7-da to 150-da, baseline 6 to 1  
tps of growth



Vil 7-da to 150-da, baseline 6 to 1  
quad trend fit



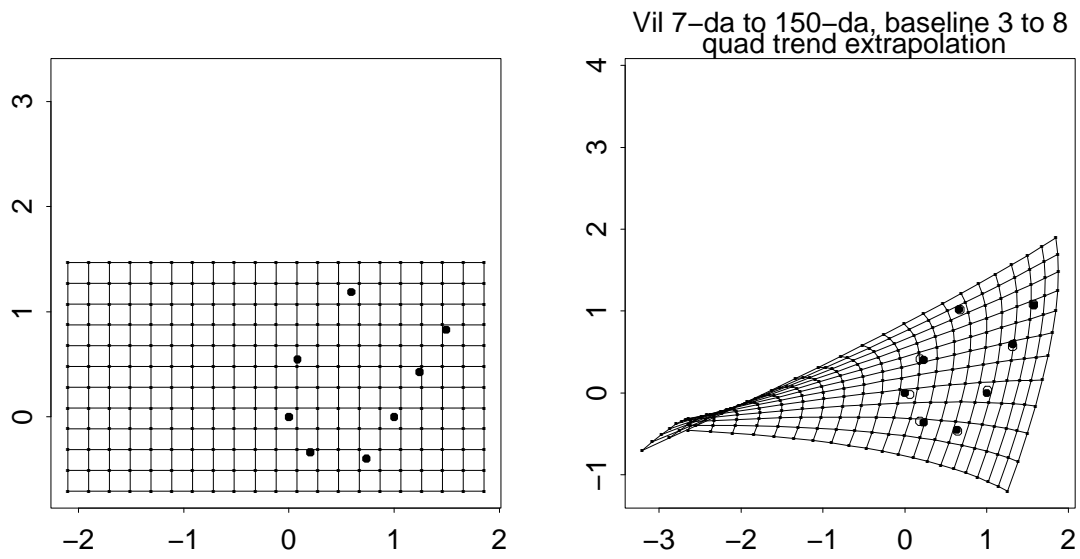


Figure 13.

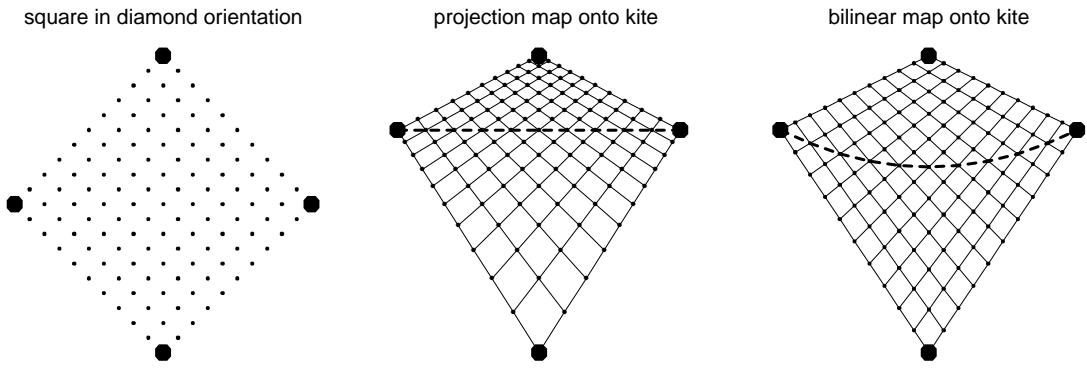


Figure 14.

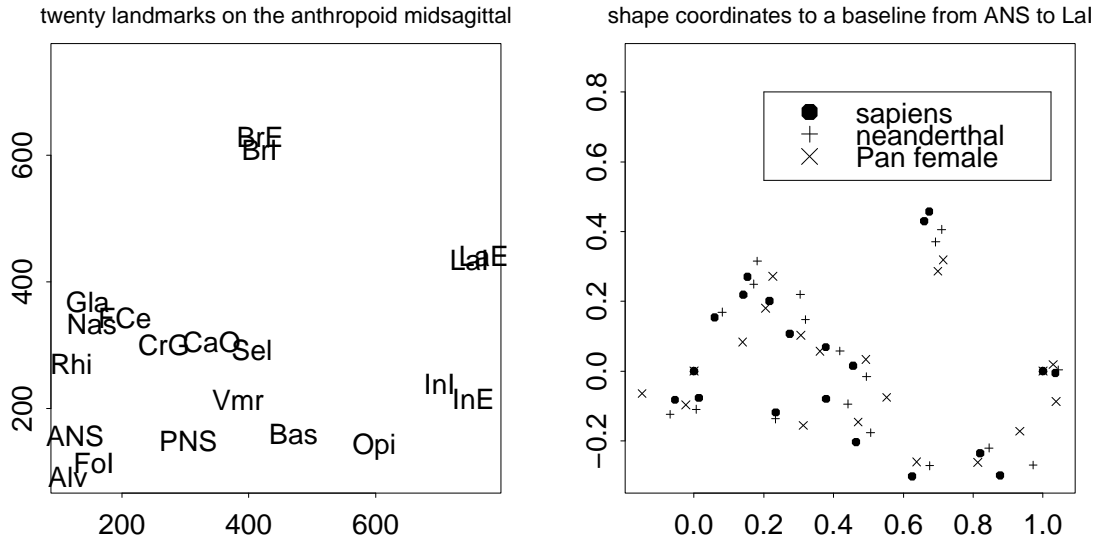
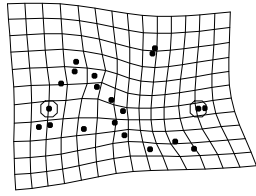


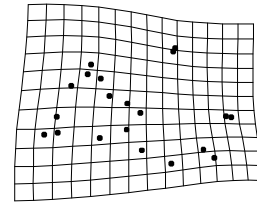
Figure 15.



H.sap. to H.neand, baseline 2 to 11  
conventional thin-plate spline



H.sap to H.neand, baseline 2 to 11  
tps of quadratic fit



H.sap to H.neand, baseline 2 to 11  
quad trend fit

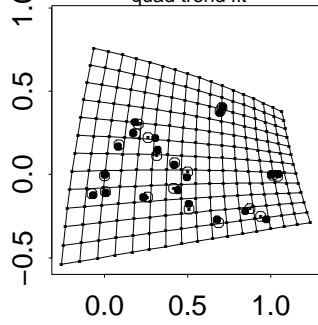
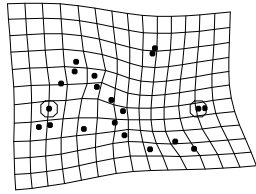
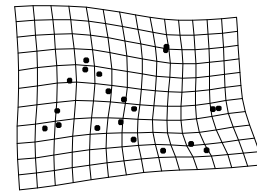


Figure 16.

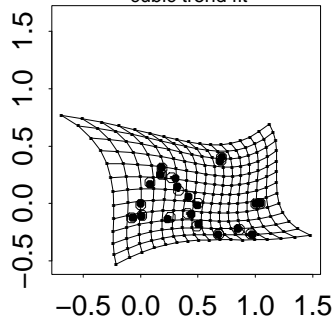
H.sap. to H.neand, baseline 2 to 11  
conventional thin-plate spline



H.sap. to H.neand, baseline 2 to 11  
tps of cubic fit



H.sap. to H.neand, baseline 2 to 11  
cubic trend fit



H.sap. to H.neand, baseline 2 to 11  
cubic trend fit, trimmed view

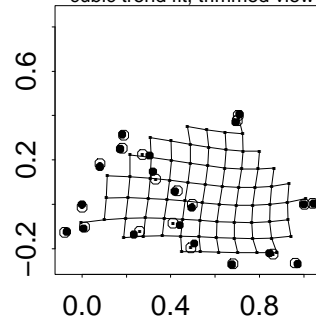
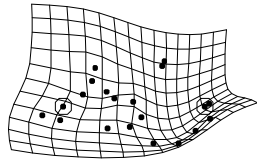
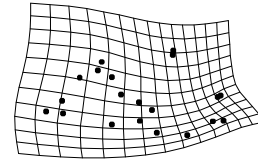


Figure 17.

H.sap. to Pan.f, baseline 2 to 11  
conventional thin-plate spline



H.sap. to Pan.f, baseline 2 to 11  
tps of quadratic fit



H.sap. to Pan.f, baseline 2 to 11  
quad trend fit

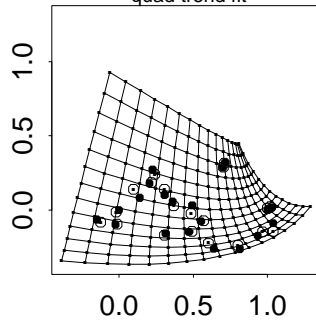
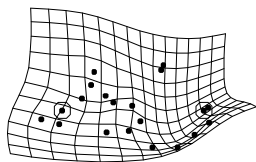
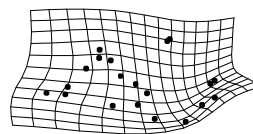


Figure 18.

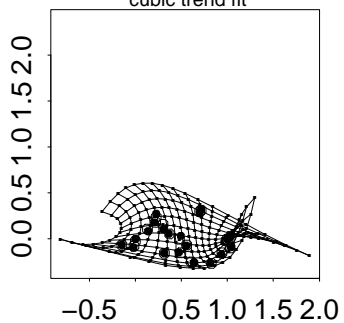
H.sap. to Pan.f, baseline 2 to 11  
conventional thin-plate spline



H.sap. to Pan.f, baseline 2 to 11  
tps of cubic fit



H.sap. to Pan.f, baseline 2 to 11  
cubic trend fit



H.sap. to Pan.f, baseline 2 to 11  
cubic trend fit, trimmed view

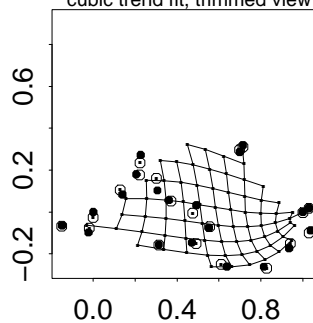


Figure 19.